IEEE Access
Multidisciplinary | Rapid Review | Open Access Journal

Received 2 March 2024, accepted 20 April 2024, date of publication 24 April 2024, date of current version 6 May 2024.

Digital Object Identifier 10.1109/ACCESS.2024.3393128

RESEARCH ARTICLE

Keyhole Porosity Identification and Localization via X-Ray Imaging With YOLO

MUHAMMAD AYUB ANSARI, ANDREW CRAMPTON, AND SIMON PARKINSON
School of Computing and Engineering, University of Huddersfield, Queengate Campus, Yorkshire, HD1 3DH Huddersfield, U.K.
Corresponding author: Muhammad Ayub Ansari (M.A.Ansari@hud.ac.uk)

ABSTRACT The advent of Additive manufacturing (AM) of 3D printed objects is revolutionising the manufacturing industry. Despite its promise, the extensive post-processing requirements of 3D objects remains a significant barrier to AM's wider adoption. Identifying defects in real-time from powder bed images taken before and after the laser melting of the current layer presents a promising strategy to reduce post-processing efforts. Traditional methods focusing on the top-layer images fall short in identifying multi-layer defects such as keyhole porosity, balling, and lack of fusion, which are critical to the integrity of 3D printed objects. Addressing this challenge, our study introduces an innovative multi-layer technique for the detection of keyhole porosity using high-quality X-ray Computed Tomography (XCT) images, leveraging the capabilities of the cutting-edge YOLO (You Only Look Once) object detection algorithm. Our findings reveal that this approach achieves a remarkable mean average precision (mAP) score of 92.585%, underscoring the efficacy of deep learning models in accurately identifying keyhole porosity across XCT images. This research not only demonstrates the potential for improving the quality and reliability of AM processes but also paves the way for reducing the dependency on labour-intensive post-processing steps.

INDEX TERMS Additive manufacturing, defect detection, deep learning, laser powder bed fusion, porosity, XCT images, YOLOv5.

I. INTRODUCTION

Laser powder bed fusion (LPBF) has been acknowledged as the most prominent and widely used additive manufacturing technique. There are numerous benefits to constructing 3D objects in an additive manner instead of mainstream destructive manufacturing. Despite the encouraging advantages, the LPBF process is not free of defects [77]. Among all the LPBF defects, porosity is the most harmful and challenging to identify, and in most cases, it is impossible to avoid [48], [49]. Many researchers have tried to identify porosity defects from various types of data such as powder bed images [58], [59], [60], [66], meltpool monitoring [63], [64], [65] and acoustic emission data [61], [62]. Many studies have used X-Ray Computed Tomography (XCT) data in their experiments as a benchmark due to its high-quality images. However, few studies have employed XCT as the primary source for in-situ porosity identification. The powder bed images are the most promising data for porosity detection in real-time during printing. Significant progress has been made in identifying porosity from powder bed images. However, porosity detection from the powder bed images is hindered mainly due to the following main factors.

1) Poor image quality.
2) Multi-layer nature of some porosity types.
3) Certain kinds of porosity can be smaller than the camera resolution.

The powder bed imaging systems in most 3D metal printers are not equipped with high-resolution cameras. High-quality camera systems are the prerequisite for accurate porosity identification from powder bed images. Some studies have mounted extra off-axis high-resolution cameras, showing that high-resolution images result in more accurate porosity identification. Experiments have discovered that some porosity types were hidden under the current layer. This meant that the captured powder layer images could not identify porosity defects in real-time, as the camera could

The associate editor coordinating the review of this manuscript and approving it for publication was Joewono Widjaja.

only capture the current layer. Lack of Fusion (LoF) porosity occurs between the previous melted and current layers [55]. Similarly, keyhole pores [56] are the result of entrapped gas porosity in the melt pool and are not visible on the top of the layer. High laser power and scan speed cause balling, a phenomenon where various melt-pools are created, and each competes to capture more of the surrounding powder and thus grow in size [57]. This creates voids amongst the melt pools and is visible on the top layer. However, the next powder layer may or may not fill these gaps. Among the porosity types, keyhole porosity is the smallest in size and more difficult to detect. Keyhole pores are round/spherical in shape and much smaller in size; typically bigger than 50 μm [73], [74], [75], [76]. Most printers' default camera resolution is bigger than the keyhole porosity. For example, the SLM500HL printer has a Baumer TGX20 camera resolution of 200 μm, while the EOS M290 printer has a default camera resolution of 100 μm. Hence, there exists a pressing need to enhance the imaging quality of the existing powder bed imaging systems or integrate in-situ X-ray imaging. XCT [50] is the most recommended and industrial standard post-build non-destructive technique for pore morphology and distribution in 3D object quality monitoring. XCT analysis results in high-quality and sharp cross-sectional images of 3D specimens. XCT imaging systems can offer remarkably high resolutions, reaching as fine as 1-2 μm, thereby addressing the current limitations and providing a valuable solution.

The shortcomings of the current methods for identifying porosity can be overcome by devising a multi-layer analysis of 3D objects via high-resolution images. The problem of low-resolution images could be overcome by utilising post-processing techniques such as XCT and Microscopy, known for their excellent image resolution. Many studies have used XCT to examine pores in the powder stock and the final 3D objects [51], [52], [53], [54]. The XCT is an ex-situ technique; therefore, it has yet to be used in the real-time identification of porosity. However, realising its potential and high-quality images, some studies [67], [68] have proposed the integration of XCT in 3D printers. Section II-A discusses the in-situ X-ray imaging systems and the quality of the captured images. Melting the top powder layer during printing modifies the material below it because of the heat exchange with previous layers and partial remelting of the last layer. Integrated XCT will assist in analysing the defects and anomalies from a multi-layer perspective.

Our previous studies [59], [66] focused on defect identification from powder bed images using XCT scanning and XCT data as a benchmark. We proposed performing a quality test of the built parts from the powder bed images using XCT, labelling different types of defects on the layer-based images and training machine learning (ML) models to automatically identify these defects from images of the powder layer surface taken before and after re-coating. In this paper, we expand our investigation of porosity from seeded porosity on low-quality powder bed images to natural, keyhole porosity identification from XCT images. Identifying pores from the XCT images benefits businesses and practitioners as it holds much commercial value. Instead of simply classifying the image, identifying the pore locations in the 3D metal objects is more commercially and practically lucrative. In real-time defect detection, merely classifying images as porosity or non-porosity fails to provide insights into the specific type or quantity of porosity present. The identification and localisation of pores are crucial for accurately quantifying porosity content. A higher number of porosity objects directly corresponds to increased porosity. This paper focuses on identifying and localising keyhole porosity, but the proposed methodology can readily be extended to encompass other porosity types, including LoF and balling.

This paper proposes an object detection approach to porosity identification from a multi-layer perspective using XCT images. We employ state-of-the-art object detection algorithms to identify and locate pores on XCT images. We printed 16 cubes on the SLM500HL printer and naturally created pores in test cubes by varying printing parameters. The XCT images of the selected cubes were carefully labelled, and pores were identified and localised using You Only Look Once (YOLO) and its different versions. The proposed framework successfully identified pores with mean average precision (mAP) of 92.585%. The rest of the paper is organised into four sections. Section two explains in-situ X-ray imaging systems and concludes by covering the recent applications of object detection algorithms in LPBF defect detection. Section three covers the experimental design and methodology. The proposed object detection framework's results and their critical evaluation are presented in chapter four. The conclusions and future work are summarised in the final section five.

II. RELATED WORK

A. IN-SITU X-RAY IMAGING SYSTEMS

The in-situ sensing and measurement techniques in LPBF record patterns and phenomena before, after, or during printing. Most sensor values, especially the powder bed imaging system, record changes at the top layer. However, each newly printed layer alters the build volume due to the heat exchange between the current and previous layers and partial remelting of the previous layer. Some researchers have devised ad-hoc printing settings to observe the effects and defects spanning multiple layers. These include subsurface melt pool dynamics and volumetric reconstruction using X-ray imaging, acoustic emissions, and base-plate deformation. One stream of research uses high-speed, high-energy X-ray imaging systems to observe subsurface melt pool dynamics, penetration depth and pore formation. References [67] and [68] explored the feasibility of in-situ micro-tomography.

X-ray imaging primarily examines the melt-pool cross-section in a plane perpendicular to the layer and provides valuable insights into the origin of various defects.

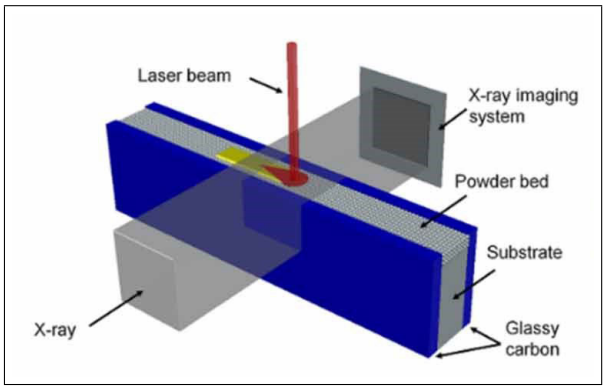

FIGURE 1. The proposed scheme of in-situ X-ray imaging system by [67].

[67] proposed an in-situ, X-ray imaging apparatus, as shown in Figure 1. A high-energy X-ray beam is passed through the material, perpendicular to both the scan and build directions. Laser scanning occurs along a narrow powder bed positioned between two transparent walls typically composed of glassy carbon sheets.

Figure 1 demonstrates that in-situ, X-ray imaging for measurements is presently confined to laboratory-scale setups featuring custom LPBF prototype systems. In-situ, X-ray imaging has helped unveil intricate dynamic changes within the melt pool and has assisted in observing various multi-layer defects. X-ray's remarkably high spatial and temporal resolution has assisted in observing and recording various defects beneath the layer. The excellent spatial resolution of 1 μm/pixel to 2 μm/pixel, coupled with a sampling rate surpassing 100,000 frames per second, was achieved with the in-situ X-ray imaging system [70], [71], [72].

Another approach proposed by [68] showcases the feasibility of in-situ, X-ray micro-tomography for the volumetric reconstruction of the part throughout the process. The top panel of Figure 2 schematically illustrates the apparatus presented in [68]'s work, and the bottom panel of Figure 2 exhibits the resulting 3D reconstruction of a wall obtained from measurements at different consecutive layers. In [68]'s study, 1500 projections were acquired during the in-situ micro-tomography scan, requiring 45 seconds for completion. The measurements presented in this research exhibited a spatial resolution of 3.64 μm/pixel and a field of view measuring (8.8 $\times$ 6.2) mm.

B. OBJECT DETECTION IN LPBF APPLICATIONS

In the literature, both one-stage and two-stage-based object detection algorithms have been used in LPBF defects detection and localisation. Reference [38] used faster R-CNN to detect helium gas bubbles in Irradiated X-750. The proposed framework was four times faster than manual analysis and acquired an accuracy of 93%. Reference [44] proposed an optimised and autonomous framework for characterising pores, particles, and grain boundaries from a microstructure image. The YOLOv5 algorithm was used for the localisation

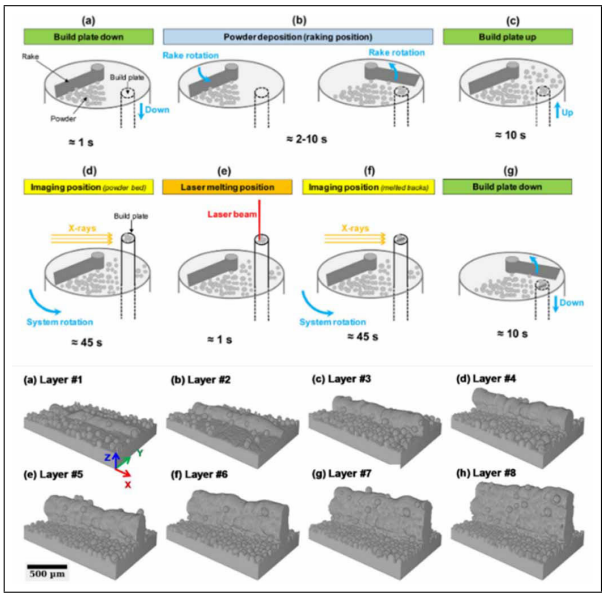

FIGURE 2. The proposed scheme of in-situ, X-ray imaging system by [68].

of pores on the images. The framework benefited from the high performance of YOLOv5 on a small dataset and used 800, 100, and 100 images for training, validation, and testing, respectively. Reference [39] employed YOLOv3, YOLOv5, and faster R-CNN for droplet detection in various microfluidic systems and experimentation. Experiments showed that YOLOv5 outperformed YOLOv3 and faster R-CNN in precise bounding box prediction. Faster R-CNN, a two-staged detector, was much slower than YOLOv5, occasionally over-fitting and missing the most prominent objects. Due to its small, compact, decent frame rate on a live high-speed camera and less hardware requirement of YOLOv5 with small weights/version was selected for droplet detection. Reference [40] has proposed a YOLO-based framework that automatically analyses the Transmission Electronic Microscope (TEM) data for defects detection in FeCrAl alloys. The proposed solution replaced the old time-consuming, laborious, and discriminatory practice of manually analysing the TEM data to quantify the in-situ defects. The YOLO-based solution achieved an F1 score of 0.89. Reference [41] using faster R-CNN to identify the location and geometry of different defects in irradiated steel. Electronic Microscopy (EM) is widely used for defects detection (pores, cavities, grain boundaries) and materials' morphological & structural properties. The EM data analysis is time-consuming, error-prone, biased, tedious, and impractical to scale. The proposed faster R-CNN solution with an F1 score of 0.78 is reliable, fast, and scalable for EM data analysis.

Apart from LPBF, object detection algorithms have been used in various disciplines. Reference [35] has used YOLOv5 to detect safety helmets at a workplace with 94.7% mean average precision (mAP). Reference [42] has also employed

YOLOv5 to detect underwater targets in side-scan sonar (SSS) images. The proposed solution achieved mAP of 85.6% and 87.8% macro F2-score. Reference [78] have used YOLOv3 and various deep learning and NLP models for automatic image captioning. Reference [43] proposed YOLO-FIR For Infrared(IR) images to solve the low resolution and big miss-classification problems in infrared images. The proposed solution is based on YOLOv5 and has 89% fewer parameters, 93% reduced size, and 62% more efficient detection time on the KAIST data set.

There are few studies focused on porosity identification using YOLO. One stage and two staged object detection algorithms were used to identify and localise various objects. All these studies showed the efficacy of object detection models. However, only a few researchers have investigated porosity identification via object detection algorithms.

III. MATERIAL AND METHODS

A. INSTRUMENT SETUP

The test specimen consisted of 16 cubes. The XCT data and the sensor files were captured and used for the experiments. The 16 printed cubes are shown in Figure 3. Previously, we experimented with powder bed images captured from 3D metal cylinders with seeded porosity manufactured with Aluminium(A20X) metal powder on an SLM SLM500HL metal printer. The current experiment consisted of 16 cubes printed on the same printer with the same Aluminium(A20X) metal powder. However, XCT images are used instead of powder bed images to investigate the smaller keyhole porosity detection due to their higher-quality. The printing setup consisted of a layer thickness = 30 μm, scan speed = 1500mm/s and laser spot size = 80 - 115 μm.

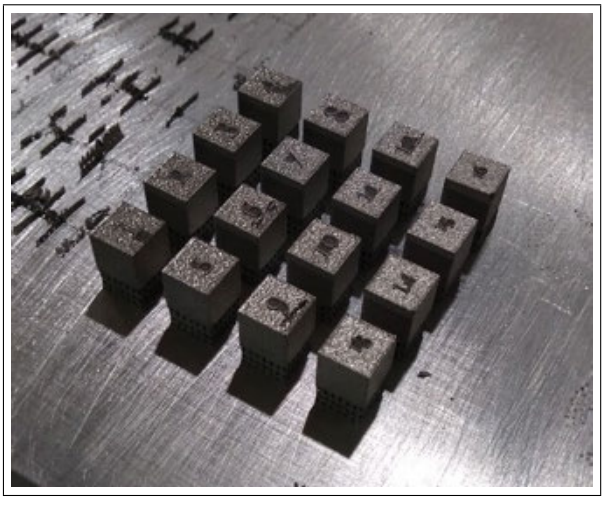

FIGURE 3. The 16 cubes of 1cm printed in SLM.

B. DESIGN OF THE EXPERIMENT

Laser power, laser spot size, scanning velocity, hatch distance, and layer thickness are the most critical processing parameters. The integrity and quality of 3D specimens rely on the correct values for these parameters. Figure 4 shows how the laser power and scan speed influence the outcome. A low laser power and high scan speed cause LoF. The laser power does not fully melt the powder layer, leaving the unfused metal powder between the current and the previously melted layer. However, high laser power and low scan speed transfer too much energy and entrap the gas in the melt pool, causing keyhole porosity. On the other hand, a high value of laser power and scan speed transfers an excessive amount of energy to the current metal powder layer. The high surface tension gradient creates small beads of the melt pool that solidify quickly, resulting in balling. Hatch spacing is the distance between two printing vectors. Low laser power and high scan speed are suitable for small hatch distances. Whereas a large hatch distance works best with high laser power and less scan speed. The goal is to find time-efficient, optimal values for the printing parameters [1].

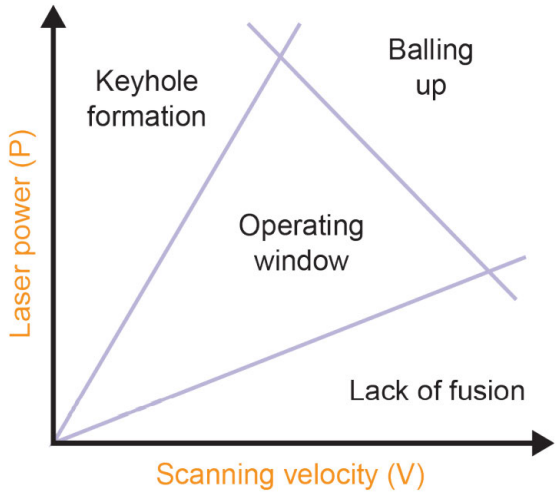

FIGURE 4. Laser Power vs Scan Speed effect on the printing process [1].

In our previous work, the experiments aimed to distinguish images with porosity from non-porosity images, irrespective of the type of porosity. Instead of focusing on porosity, identifying the exact porosity type is a highly practical and realistic requirement. Doing so will assist the printer operator in adjusting the appropriate printing parameters to limit or avoid anomalies during printing. For example, LoF can occur when the laser power is inadequate to fully melt the powder layer. Real-time detection and notification of LoF occurrences during printing would enable printer operators to adjust the laser power to prevent LoF porosity promptly. Therefore, having precise knowledge of the specific type of porosity is highly advantageous for taking corrective measures and effectively mitigating the occurrence and extent of porosity. The experiments in this study were designed to identify the exact porosity type. The printing parameters were chosen appropriately to create LoF and keyhole porosity. Sixteen cubes of 10mm were designed to study the effect of various parameter settings on natural porosity creation. Each cube was printed with different values of hatch spacing

TABLE 1. Printing parameter settings for cubes and their densities.

Cube ID	Hatch Spacing (mm)	Laser Power (W)	Energy Density (J/mm^3)	Density (%)
1	0.1	400	88.89	99.94 ± 0.01
2	0.13	400	68.38	100.01 ±0.26
3	0.16	400	55.56	100.05 ±0.26
4	0.19	400	46.78	99.20 ± 0.36
5	0.1	350	77.78	100.16 ± 0.00
6	0.13	350	59.83	99.94 ± 0.27
7	0.16	350	48.61	99.23± 0.46
8	0.19	350	40.94	98.72 ± 0.27
9	0.1	300	66.67	100.19 ± 0.62
10	0.13	300	51.28	99.88 ±0.53
11	0.16	300	41.67	98.92 ± 0.35
12	0.19	300	35.09	97.91 ±0.04
13	0.1	250	55.56	99.76 ± 0.02
14	0.13	250	42.74	99.37 ± 0.18
15	0.16	250	34.72	98.06 ± 0.02
16	0.19	250	29.24	96.48 ± 0.17

and laser power. The energy density was also measured. The percentage of porosity in each cube was measured using Archimedes' density measurement.

Different values of two important processing parameters, hatch spacing and laser power, were used to observe their effect on porosity creation. The complete parameter settings for sixteen cubes, along with their energy densities and density percentage, are shown in Table 1. The hatch spacing values of 0.1, 0.13, 0.16, and 0.19 were combined with 400, 350, 300, and 250 laser power values. A 3D metal object with 100 % density means the object has no porosity. Whereas less dense objects have porous interiors.

For the porosity calculation, we employed Archimedes' density measurement principle. The weight of the 3D objects was measured in the air and by submerging them in a liquid. The porous objects are less dense. So, measuring the density of the objects provides the degree of porosity in them.

C. DATA CAPTURE

Energy density is the amount of heat/energy transferred per unit area. The melt-pool shape, size, and width are dependent on the energy density. Energy density is calculated as

$$E = \frac{P}{v \times h \times t}. \tag{1}$$

where E is the energy density, P is laser power in watts (W), v is the scan speed in millimetres per second (mm/s), h is hatch spacing in (mm), and t is the layer thickness in (mm). Energy density directly influences the final density of the 3D object. It can be observed in Figure 5. The Figure confirmed that the experiments were designed with varying values of printing parameters. The density of the 3D objects increased with the increased energy density. However, increasing the energy density beyond the optimal threshold results in porous or less dense objects. The effect of the laser power and hatch spacing printing parameters on the object's density is shown in Figure 6 and Figure 7, respectively. The density of 3D specimens depends on various factors. Therefore, observing the effect of a single printing parameter on the object's density could be misleading. In our experiments, the density of the cubes increased with the increase in laser power. However, it could be observed that different cubes have different densities at the same laser power. This is because of the same reason that the density of objects depends on various printing parameters. Increasing the hatch spacing decreased the density of the cubes. A bigger/wider hatch spacing between printing tracks would require more energy and a bigger laser spot size to melt the metal powder fully. However, like most experiments, laser spot size was fixed in our experiments, which is why increasing the hatch spacing results in less dense cubes.

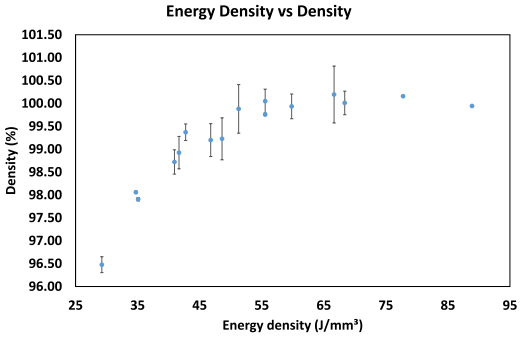

FIGURE 5. Effect of energy density on the density of the 3D object.

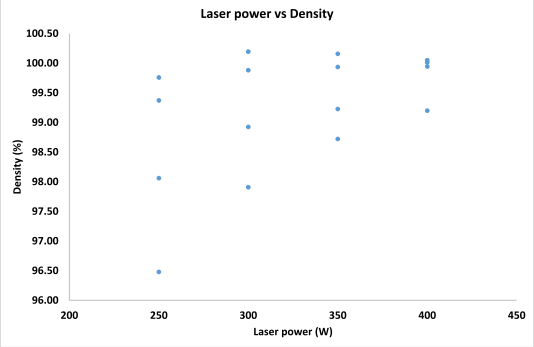

FIGURE 6. Effect of laser power on the density of 3D object.

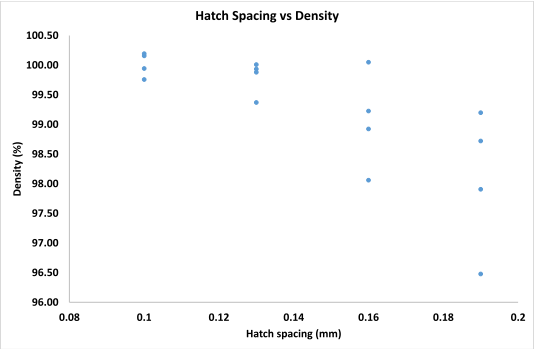

FIGURE 7. Effect of hatch spacing on the density of 3D object.

The energy density of the sixteen cubes is shown in Table 1. The maximum energy density value was 88.89, with laser power = 400 and hatch spacing = 0.1. The minimum energy density of 29.24 was computed for the low laser power 250 and a wide hatch spacing of 0.19. Out of the sixteen cubes, four cubes were shortlisted based on the energy density values.

Cube 1, 7, 9, and 16 were shortlisted for XCT scanning as scanning all sixteen cubes is expensive and time-consuming. The sample cubes numbered 1, 7, 9, and 16 had percentage densities of 99.94, 99.23, 100, and 96.48, respectively. A sample XCT image from each of the four selected cubes is shown in Figure 8. The energy densities of cubes 1 and 9 are 88.89 and 66.67, respectively. Both cubes have high density and show minimal porosity. Cube 16 has the lowest energy density and hence the least density and more porosity. Cube 16 showed a high rate of porosity. Cubes 1, 9, and 16 could be considered extreme scenarios with extremely low and high values. However, cube 7 is closer to a realistic case. Cube 7 has an energy density of 48.61 and achieved an excellent density percentage. The printing parameter values for cube 7 lie close to the operating window. We selected cube 7 for the porosity identification and localisation.

D. DATA LABELLING

Preparing the object recognition data set is challenging and time-consuming. A bounding box needs to be drawn around each pore on the XCT image. Various software tools and

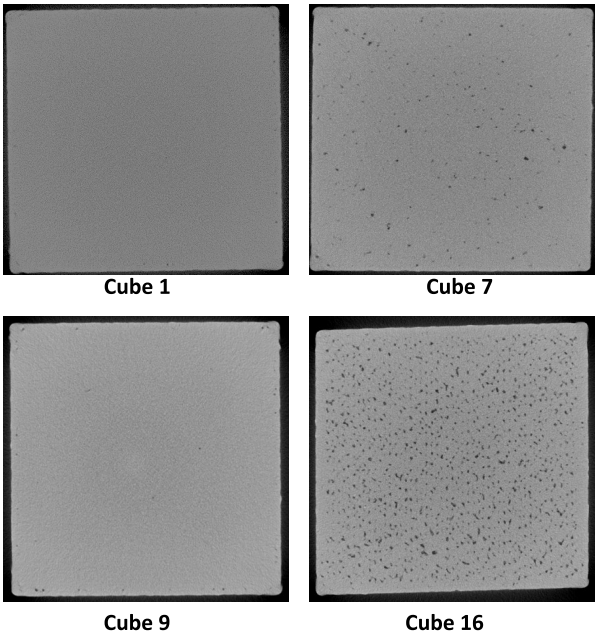

FIGURE 8. A sample XCT image of each selected cube.

Python libraries are used to prepare the image data set for object recognition algorithms. An open-source, custom-built Python library called "labelimg" [2] was used to draw the bounding boxes around the pores. The bounding box information, such as X and Y coordinates, labels, and types, is stored in a separate XML file. This way of labelling is more professional and compatible with the Python platform than other software tools. The XCT scan of a single cube resulted in 1800 images. The number of pores per image ranges from 50 to 300, and it takes roughly 5 to 20 minutes to draw the bounding boxes and assign labels. Labelling all the images would take a considerable amount of time and effort. Therefore, it is prudent to label a sufficient amount of data and test the viability of the experimental approach rather than investing substantial time and effort only to discover fundamental flaws in the chosen direction later. Due to this task's substantial time and labour requirements, we had to limit our experiments to focusing solely on keyhole porosity detection. The data set consisted of 74 images. The images were taken from different cross-sectional areas of cube 7. Of 74 images, 52 were used for training and 15 for validation. Seven images were kept separate and were never exposed to the model during the training phase. Once the model is trained or fine-tuned, the model is then tested on the reserved 7 test images. A typical train test splitting mechanism of a data set is shown in Figure 9. The data set comprised 31,123 porosity objects. The number of images is small in the data set, but the number of objects to identify is sufficiently large. Drawing a precise bounding box around porosity can be time-consuming due to its typically small size. Moreover, only keyhole porosity was formed on the captured images.

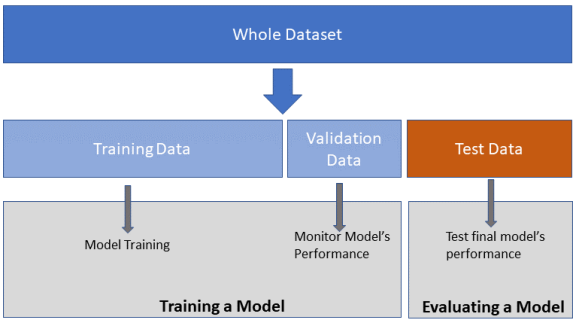

FIGURE 9. Typical splitting of data sets.

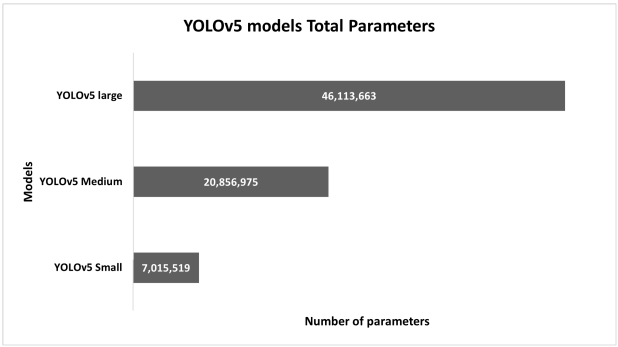

FIGURE 10. Total parameters in YOLOv5 models.

TABLE 2. Models summary.

Model	Layers	Parameters	Inference Time
YOLOv5 Small	213	7,015,519	0.028
YOLOv5 Medium	290	20,856,975	0.055
YOLOv5 Large	367	46,113,663	0.033

E. YOLOV5

You Only Look Once (YOLO) [3], R-CNN [4] and Single Shot Detector (SSD) [5] are the most established and widespread object recognition family of algorithms. The choice of object recognition model is mostly based on the model's accuracy and detection speed. YOLO algorithms are surprisingly fast, and their latest versions are accurate and precise. YOLOv5 is the latest version of the YOLO family of models, and it is known for its reduced memory requirements and exportability. YOLOv5 is proposed by Ultralytics [69]. There is no formal peer-review paper on YOLOv5; it is only shared on GitHub. The only improvement of YOLOv5 over its previous version is including the anchor box selection process in the model. YOLOv5 does not need a pre-trained model; instead, it can learn the most appropriate anchor boxes from the data set during training. YOLOv5 is much lighter and faster than its predecessors and is used in various applications [33], [34], [35], [36]. We used YOLOv5 to identify keyhole pores. The pre-trained YOLOv5 has four different sub-versions based on the models' size. We experimented with small, medium, and large versions of YOLOv5. The number of layers and parameters in each model is shown in Table 2. Most deep learning models are based on neural network architectures comprising various stacked layers. Each type of layer (convolutional, pooling, dense etc.) has different parameters (number of neurons, filters, kernels etc.) that define the model's complexity and learning capabilities.

YOLOv5 small has only 7 million parameters. Whereas the medium and large versions have 20.8 and 46.11 million parameters, respectively. The models and their parameters are visualised for a better comparison in Figure 10.

F. EVALUATION METRICS

Evaluation metrics for object detection algorithms differ slightly from image classification tasks. The commonly used metrics are precision, recall, and mean average precision (mAP) at different Intersection over Union (IoU) values. For object detection tasks, precision and recall metrics are calculated in a similar way to those for image classification. However, the definition of true negative differs slightly from most object detection algorithms; as we do not have a false negative. Precision is the number of true positives among all the detection's made by the model. In comparison, recall is the ratio of true positives and all ground-truth values.

$$Precision = \frac{TP}{TP + FP} \tag{2}$$

$$Recall = \frac{TP}{TP + FN} \tag{3}$$

Understanding IoU is essential for the mAP metric. IoU, in object detection tasks, is the amount of overlap between ground truth and the model's prediction. It is calculated as,

$$\text{IoU} = \frac{\text{area of overlap}}{\text{area of union}} \tag{4}$$

IoU ranges in values from 0 to 1. IoU $= 1$ if the ground truth and prediction overlap entirely, and IoU $= 0$ if there is no overlap between the ground truth and the predicted bounding boxes. An acceptable overlapping threshold value is often set for ground truth and prediction boxes. For instance, an IoU at a threshold of 50%, an object detection will be considered true positive if the IoU $>$ 50%. For general purposes, a threshold is usually represented by α. A usual output of an object detection model is the bounding box, class label, and confidence score. Like a threshold for IoU, the threshold value also affects the confidence score. Large threshold values for a confidence score would result in more false negatives (missing more objects and having high precision and low recall). At the same time, a small threshold value would result in more false positives (FPs), resulting in low precision and high recall of the model. The precision-recall curve is nothing but a precision vs recall plot at different confidence scores.

The average precision (AP) at α is the area under the precision-recall curve at IoU threshold $= \alpha$. It is given by,

$$AP@\alpha = \int_0^1 P(r)\, dr. \tag{5}$$

Average precision @ α is the AP at α IoU threshold. So, AP@0.5 means the average precision at IoU = 50%. Mean average precision (mAP) is all classes' average AP values. The average precision is calculated for each class in the data sets. The number of APs equals the number of classes in the data set. The mean average precision is the average of all the APs and is a better overall metric for model evaluation. It is given by,

$$mAP@\alpha = \frac{1}{n}\sum_{i=1}^{n} AP_i \tag{6}$$

Here n is the number of classes in the data set.

IV. RESULTS AND DISCUSSION

The experiments were carried out on Google Colab, short for collaboration, an online platform. Google provides free 12GB INVIDIA Tesla GPU and support for various ML programming libraries [45]. YOLOv5 is implemented in the PyTorch [46] Python programming library. PyTorch is one of the most popular ML libraries, and it is compatible with CUDA NVIDIA GPU operations to accelerate the training operation of deep ML models [47].

A. MODEL EVALUATION AND TRAINING TIME

The three versions of YOLOv5 were trained on the same data set to identify and locate porosity from XCT images. The models were evaluated using precision, recall and mAP at two different IoU thresholds. The performance of the models is shown in Table 3. The precision of small, medium and large versions of YOLOv5 is shown in Figure 11. The precision is the ratio of true positives and all the detections made by the model. YOLOv5 medium achieved the highest precision score of 88.0%. The medium version of YOLOv5 made fewer detections (bounding boxes) and thus had the highest precision but lowest recall among small and large versions of YOLOv5. Whereas small and large versions had precision scores of 87.5% and 87.2%, respectively. It was observed that the small and large version model's precision increased gradually with each training iteration, as depicted in Figure 11. Whereas the medium version had a sharp increase in precision at the initial epochs. There is a minimal difference in the precision value of all the models, and all acquired an acceptable precision in identifying pores on the XCT images.

In terms of recall, the large version achieved the best score of 89.4%. The medium and small versions acquired a recall of 87.8% and 88.3%, respectively. A comparison of recall values amongst the three models is presented in Figure 12. A similar trend was observed in recall as that of precision. Small and large version models had comparatively slow learning than the medium version. However, the large version acquired the best recall score; probably due to having more parameters. A slight decreasing trend in recall values was revealed compared to the number of parameters in the models. The current experiments established that recall scores increased with the increase in model complexity, number of layers and parameters.

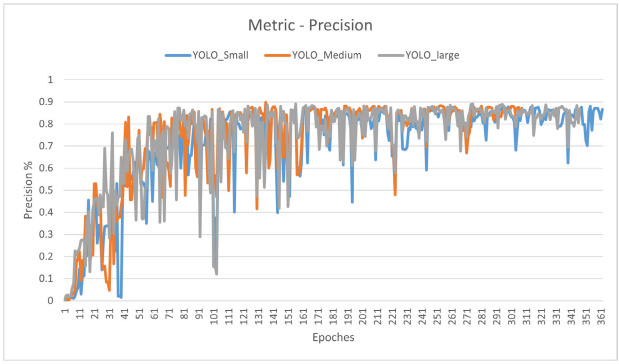

FIGURE 11. Comparison of precision of small, medium, and large versions of YOLOv5.

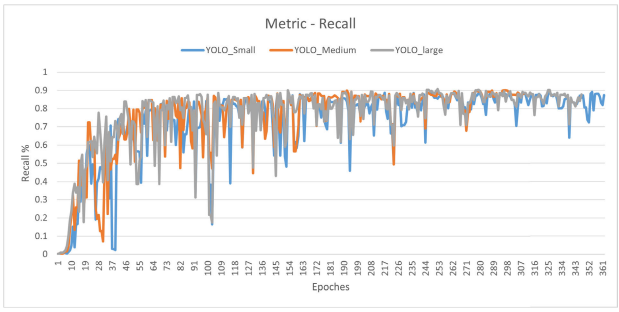

FIGURE 12. Comparison of recall of small, medium, and large versions of YOLOv5.

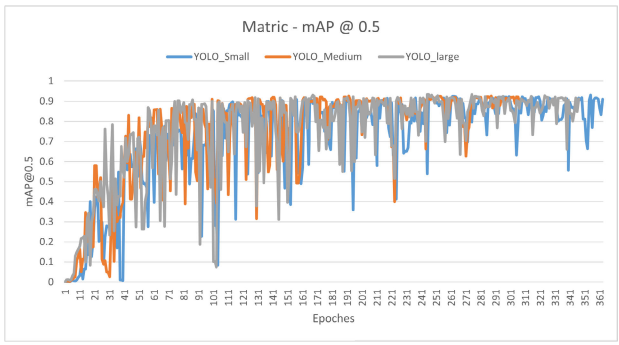

FIGURE 13. Comparison of mAP at IoU = 0.5 for small, medium, and large versions of YOLOv5.

The models were also compared and evaluated in terms of mean average precision at IoU = 50%. A predicted bounding box was considered a true positive if the area of IoU was 50% or more between the ground truth and the prediction. YOLOv5 small achieved the highest value of 92.5% of mAP@0.5. At the same time, medium and large versions also acquired excellent mAPs of 91.1% and 92.1%, respectively. Figure 13 shows the mean average precision of all models. YOLOv5 small attained a remarkable average precision of 92.5% in locating the pores from the XCT images.

TABLE 3. Model evaluation comparison.

Model	Precision (%)	Recall (%)	mAP@0.5	mAP@0.5:0.95
YOLOv5_Small	87.5	88.3	92.5	39.5
YOLOv5_Medium	88.0	87.8	91.1	41.1
YOLOv5_Large	87.2	89.4	92.1	41.2

TABLE 4. Model's training time, size, and the number of epochs.

Model	Epochs	Training Time	Model Size
YOLOv5_Small	362	35.10 min	14.5 MB
YOLOv5_Medium	309	30.12 min	42.2 MB
YOLOv5_Large	347	34.02 min	92.8 MB

It was observed that the smaller version of YOLOv5 required more training epochs. The training epochs, total training time, and the final model size of all the models are shown in Table 4. All the models were initially set to train for 1000 epochs coupled with early stopping with the patience of 100 epochs. The early stopping with the patience of 100 epochs meant that the model's training would be halted if there were no improvements in the model's training for 100 consecutive training epochs. The small version trained for 362 epochs and took 35.1 minutes. The final model size was 14.5 megabytes (MB). The medium model took 30.12 minutes with 309 epochs for its training. The large model's training was completed in 34.02 minutes after 347 training epochs. The experiments revealed that bigger models (medium and large) with more training parameters would train faster than a smaller version of YOLOv5. The smaller models, probably due to having a less complex architecture and fewer layers and parameters, require more training and time.

B. MODEL TESTING AND CRITICAL EVALUATION

The models were tested on a test data set. The models were never exposed to the test images during their training. The test data set consisted of 7 images containing 951 pore objects. The test images were passed through the models with an IoU threshold of 45% and a confidence threshold of 10%. The low confidence score was due to the small difference between pores and the surrounding melted metal powder. The total number of objects predicted by each model is shown in Table 5. Seven test images and the total number of ground truths are listed in the table. The predictions made by each model are shown against each test image.

TABLE 5. Correctly predicted objects per test image.

Test Image	Ground Truth	Predicted		
		YOLOv5 Small	YOLOv5 Medium	YOLOv5 Large
Image1	76	69	95	81
Image2	90	82	87	77
Image3	93	61	58	52
Image4	83	55	63	49
Image5	70	55	70	65
Image6	280	217	264	229
Image7	259	214	217	239
Total	951	753	854	792

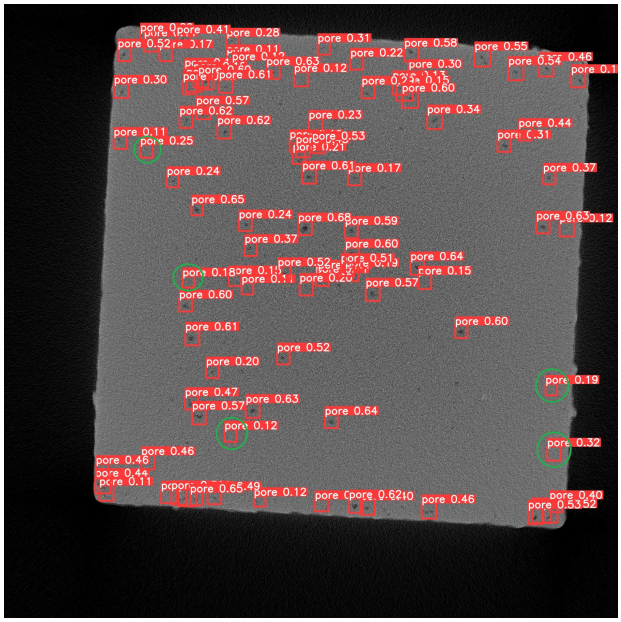

FIGURE 14. Test image 2 where YOLOv5 medium model predicted 78 objects/bounding boxes.

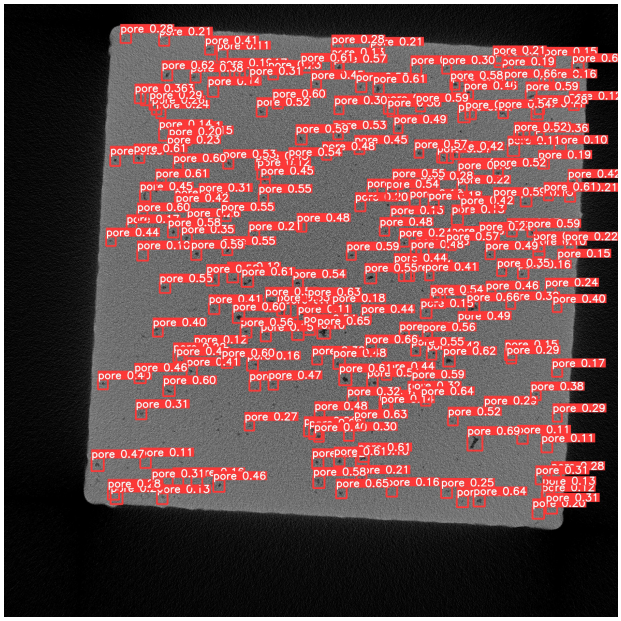

FIGURE 15. Test image 6 where the YOLOv5 medium model predicted 239 object/bounding boxes.

Out of a total of 951 ground-truth, small, medium, and large models predicted 753, 854, and 792, respectively. It is worth noting that the models' total predictions consisted of

both true positives and false positives. The YOLOv5 medium model made the most predictions of 854. Figure 15 shows the predictions made by the medium model. The model successfully identified most pores on the image with an excellent confidence score. The model missed a few pores, but the predictions were accurate and precise overall. Test image 6 (in Table 5) had pores of various sizes. Experiments revealed that the model quickly identified bigger pores and had higher confidence scores than small ones. There must be some false positive predictions, but it is difficult to observe in test image 6 due to the high number of pores. Figure 14 showed test image 2 (in Table 5) along with the predictions made by the YOLOv5 medium model. The model predicted the presence of pores in bounding boxes circled with green circles, but there were no pores. The bounding boxes with green circles around them are false positives.

The pores vary in size in the data set. XCT images are of high resolution and better quality. The XCT analysis even captured small pores that, in practice, could easily be ignored. The models performed well and achieved remarkable precision, recall and mean average precision values. All models made some mistakes too. They failed to identify and locate some pores and, at the same time, produced some false positive predictions. The number of false positives and false negatives is significantly smaller than the models' true positive predictions. Although the medium model predicted the most pores and bounding boxes, counting the exact number of TP, TN, and FP is challenging. Therefore, mean average precision at IoU@0.5 was chosen as the decisive evaluation metric. The YOLOv5 small model achieved the highest mAP and is the best choice for the problem.

Some of the wrong predictions by the YOLO models were mainly due to the tiny size of pores. Moreover, the labelling could be improved significantly. The bounding boxes should be drawn as close to the object as possible. The current labels lack this trait. Moreover, some microscopic and hardly visible pores should not be considered pores. These improvements in the labelling step would significantly improve the model's performance.

V. CONCLUSION

Detecting porosity in LPBF presents a critical and formidable challenge. In our previous papers, we identified porosity from powder bed images. After extensive hyper-parameter tuning, the proposed deep CNN was constructed from scratch and optimised. The model successfully classified powder porosity images from normal images. Powder bed images are low quality and lack clear definition due to poor lighting and a low-resolution camera inside the build chamber. The current experiments were designed to overcome these shortcomings and identify & localise porosity from superior-quality XCT images using a multi-layer approach. Sixteen cubes were printed on an SML500HL printer, and porosity defects were created naturally by varying the printing parameters. We employed three versions of the state-of-the-art YOLOv5 object detection algorithm to detect porosity from XCT images. The experiments revealed that the YOLOv5 small model is most suited for porosity detection from XCT images. The models were evaluated on precision, recall, and mAP values, and our model achieved a mAP@0.5 of 92.585%. The experiments established the foundation of deep ML applications in real-time monitoring and controlling of the LPBF process. The proposed YOLOv5-based real-time object detection solution will help AM practitioners to utilise the enormous XCT data concisely and efficiently.

Despite the excellent and promising results, the current methodology has the following limitations.

1) The proposed methodology, in terms of a multi-layer approach, is currently presented as a proof of concept. It should be noted that the XCT images were acquired after the printing process. However, considering the integration of in-situ X-ray imaging, the proposed methodology shows promising potential for practical in-situ implementation.
2) A limitation of the current work is that it focuses solely on identifying keyhole porosity. This choice was driven by the challenges associated with time-consuming and laborious data labelling. However, future studies will encompass a broader range of labelled data to encompass various types of porosities.
3) Another consideration is the need to expand the scope of labelled data to include a more comprehensive range of porosity types. This expansion will enhance the generalizability and robustness of the proposed methodology when applied to real-world scenarios.

It is important to address these limitations and continue exploring further avenues for improvement to enhance the methodology's applicability and effectiveness. The future experiments will comprehensively compare state-of-the-art, two-stage and one-stage models. Moreover, given the high-quality cameras, the same solution will be used to identify porosity and relevant defects in real-time from high-quality powder bed images. We are devising semi-automated labelling approaches utilizing fundamental image processing techniques such as histogram analysis, image binarization, connected component analysis, and edge detection. We have made notable progress in this regard and anticipate employing more labelled data through our semi-automated labelling approach in future works. These efforts will encompass various defects, including keyhole porosity, lack of fusion, and balling. Future experiments will also employ various sophisticated deep-learning techniques to improve the model's performance further.

REFERENCES

[1] M. Saunders, "X marks the spot-find ideal process parameters for your metal AM parts," White Papers Collection-Renishaw Plc, Renishaw, U.K., 2017.
[2] Tzutalin LabelImg. (2015). *Free Software: MIT License*. [Online]. Available: https://github.com/tzutalin/labelImg

[3] J. Redmon, S. Divvala, R. Girshick, and A. Farhadi, "You only look once: Unified, real-time object detection," in *Proc. IEEE Conf. Comput. Vis. Pattern Recognit. (CVPR)*, Jun. 2016, pp. 779–788.

[4] R. Girshick, J. Donahue, T. Darrell, and J. Malik, "Rich feature hierarchies for accurate object detection and semantic segmentation," in *Proc. IEEE Conf. Comput. Vis. Pattern Recognit.*, Mali, Jun. 2014, pp. 580–587.

[5] W. Liu, D. Anguelov, D. Erhan, C. Szegedy, S. Reed, C.-Y. Fu, and A. C. Berg, "SSD: Single shot multibox detector," in *Proc. Eur. Conf. Comput. Vis.*, 2016, pp. 21–37.

[6] R. Girshick, "Fast R-CNN," in *Proc. IEEE Int. Conf. Comput. Vis. (ICCV)*, Dec. 2015, pp. 1440–1448.

[7] S. Ren, K. He, R. Girshick, and J. Sun, "Faster R-CNN: Towards real-time object detection with region proposal networks," 2015, *arXiv:1506.01497*.

[8] K. He, G. Gkioxari, P. Dollár, and R. Girshick, "Mask R-CNN," in *Proc. IEEE Int. Conf. Comput. Vis. (ICCV)*, Oct. 2017, pp. 2961–2969.

[9] P. Viola and M. Jones, "Rapid object detection using a boosted cascade of simple features," in *Proc. IEEE Comput. Soc. Conf. Comput. Vis. Pattern Recognit. (CVPR)*, vol. 1, 2001, pp. I–I.

[10] D. G. Lowe, "Object recognition from local scale-invariant features," in *Proc. 7th IEEE Int. Conf. Comput. Vis.*, vol. 2, Sep. 1999, pp. 1150–1157.

[11] N. Dalal and B. Triggs, "Histograms of oriented gradients for human detection," in *Proc. IEEE Comput. Soc. Conf. Comput. Vis. Pattern Recognit. (CVPR)*, vol. 1, 2005, pp. 886–893.

[12] T. Ojala, M. Pietikainen, and T. Maenpaa, "Multiresolution gray-scale and rotation invariant texture classification with local binary patterns," *IEEE Trans. Pattern Anal. Mach. Intell.*, vol. 24, no. 7, pp. 971–987, Jul. 2002.

[13] J. Sivic and A. Zisserman, "Video Google: A text retrieval approach to object matching in videos," in *Proc. 9th IEEE Int. Conf. Comput. Vis.*, vol. 3, Oct. 2003, pp. 1470–1477.

[14] Y. Cheng, D. Wang, P. Zhou, and T. Zhang, "Model compression and acceleration for deep neural networks: The principles, progress, and challenges," *IEEE Signal Process. Mag.*, vol. 35, no. 1, pp. 126–136, Jan. 2018.

[15] S. Lazebnik, C. Schmid, and J. Ponce, "Beyond bags of features: Spatial pyramid matching for recognizing natural scene categories," in *Proc. IEEE Comput. Soc. Conf. Comput. Vis. Pattern Recognit. (CVPR)*, vol. 2, Jun. 2006, pp. 2169–2178.

[16] F. Perronnin, J. Sánchez, and T. Mensink, "Improving the Fisher kernel for large-scale image classification," in *Proc. Eur. Conf. Comput. Vis.*, 2010, pp. 143–156.

[17] A. Krizhevsky, I. Sutskever, and G. E. Hinton, "ImageNet classification with deep convolutional neural networks," in *Proc. Adv. Neural Inf. Process. Syst.*, vol. 25, 2012, pp. 1–9.

[18] K. Simonyan and A. Zisserman, "Very deep convolutional networks for large-scale image recognition," 2014, *arXiv:1409.1556*.

[19] C. Szegedy, W. Liu, Y. Jia, P. Sermanet, S. Reed, D. Anguelov, D. Erhan, V. Vanhoucke, and A. Rabinovich, "Going deeper with convolutions," in *Proc. IEEE Conf. Comput. Vis. Pattern Recognit. (CVPR)*, Jun. 2015, pp. 1–9.

[20] O. Russakovsky, J. Deng, H. Su, J. Krause, S. Satheesh, S. Ma, Z. Huang, A. Karpathy, A. Khosla, M. Bernstein, A. C. Berg, and L. Fei-Fei, "ImageNet large scale visual recognition challenge," *Int. J. Comput. Vis.*, vol. 115, no. 3, pp. 211–252, Dec. 2015.

[21] M. Tan and Q. Le, "EfficientNet: Rethinking model scaling for convolutional neural networks," in *Proc. 36th Int. Conf. Mach. Learn.*, 2019, pp. 6105–6114.

[22] K. He, X. Zhang, S. Ren, and J. Sun, "Deep residual learning for image recognition," in *Proc. IEEE Conf. Comput. Vis. Pattern Recognit. (CVPR)*, Jun. 2016, pp. 770–778.

[23] K. He, X. Zhang, S. Ren, and J. Sun, "Identity mappings in deep residual networks," in *Proc. Eur. Conf. Comput. Vis.*, 2016, pp. 630–645.

[24] P. Felzenszwalb, D. McAllester, and D. Ramanan, "A discriminatively trained, multiscale, deformable part model," in *Proc. IEEE Conf. Comput. Vis. Pattern Recognit.*, Jun. 2008, pp. 1–8.

[25] J. R. R. Uijlings, K. E. A. van de Sande, T. Gevers, and A. W. M. Smeulders, "Selective search for object recognition," *Int. J. Comput. Vis.*, vol. 104, no. 2, pp. 154–171, Sep. 2013.

[26] K. He, X. Zhang, S. Ren, and J. Sun, "Spatial pyramid pooling in deep convolutional networks for visual recognition," *IEEE Trans. Pattern Anal. Mach. Intell.*, vol. 37, no. 9, pp. 1904–1916, Sep. 2015.

[27] S. Ren, K. He, R. Girshick, and J. Sun, "Faster R-CNN: Towards real-time object detection with region proposal networks," in *Proc. Adv. Neural Inf. Process. Syst.*, vol. 28, 2015, pp. 1–9.

[28] C. L. Zitnick and P. Dollár, "Edge boxes: Locating object proposals from edges," in *Proc. Eur. Conf. Comput. Vis.*, 2014, pp. 391–405.

[29] J. Redmon and A. Farhadi, "YOLO9000: Better, faster, stronger," in *Proc. IEEE Conf. Comput. Vis. Pattern Recognit. (CVPR)*, Jul. 2017, pp. 7263–7271.

[30] J. Redmon, "DarkNet: Open source neural networks," Tech. Rep., 2013.

[31] K. He, X. Zhang, S. Ren, and J. Sun, "Delving deep into rectifiers: Surpassing human-level performance on ImageNet classification," in *Proc. IEEE Int. Conf. Comput. Vis. (ICCV)*, Dec. 2015, pp. 1026–1034.

[32] A. Bochkovskiy, C.-Y. Wang, and H.-Y. Mark Liao, "YOLOv4: Optimal speed and accuracy of object detection," 2020, *arXiv:2004.10934*.

[33] H. Wang, S. Zhang, S. Zhao, Q. Wang, D. Li, and R. Zhao, "Real-time detection and tracking of fish abnormal behavior based on improved YOLOV5 and SiamRPN++," *Comput. Electron. Agricult.*, vol. 192, Jan. 2022, Art. no. 106512.

[34] Y. Jing, Y. Ren, Y. Liu, D. Wang, and L. Yu, "Automatic extraction of damaged houses by earthquake based on improved YOLOv5: A case study in yangbi," *Remote Sens.*, vol. 14, no. 2, p. 382, Jan. 2022.

[35] F. Zhou, H. Zhao, and Z. Nie, "Safety helmet detection based on YOLOv5," in *Proc. IEEE Int. Conf. Power Electron., Comput. Appl. (ICPECA)*, Jan. 2021, pp. 6–11.

[36] X. Zhu, S. Lyu, X. Wang, and Q. Zhao, "TPH-YOLOv5: Improved YOLOv5 based on transformer prediction head for object detection on drone-captured scenarios," in *Proc. IEEE/CVF Int. Conf. Comput. Vis. Workshops (ICCVW)*, Oct. 2021, pp. 2778–2788.

[37] X. Wu, D. Sahoo, and S. C. H. Hoi, "Recent advances in deep learning for object detection," *Neurocomputing*, vol. 396, pp. 39–64, Jul. 2020.

[38] C. M. Anderson, J. Klein, H. Rajakumar, C. D. Judge, and L. K. Béland, "Automated detection of helium bubbles in irradiated X-750," *Ultramicroscopy*, vol. 217, Oct. 2020, Art. no. 113068.

[39] G. P. Rutkowski, I. Azizov, E. Unmann, M. Dudek, and B. A. Grimes, "Microfluidic droplet detection via region-based and single-pass convolutional neural networks with comparison to conventional image analysis methodologies," *Mach. Learn. Appl.*, vol. 7, Mar. 2022, Art. no. 100222.

[40] M. Shen, G. Li, D. Wu, Y. Yaguchi, J. C. Haley, K. G. Field, and D. Morgan, "A deep learning based automatic defect analysis framework for in-situ TEM ion irradiations," *Comput. Mater. Sci.*, vol. 197, Sep. 2021, Art. no. 110560.

[41] M. Shen, G. Li, D. Wu, Y. Liu, J. R. C. Greaves, W. Hao, N. J. Krakauer, L. Krudy, J. Perez, V. Sreenivasan, B. Sanchez, O. Torres-Velázquez, W. Li, K. G. Field, and D. Morgan, "Multi defect detection and analysis of electron microscopy images with deep learning," *Comput. Mater. Sci.*, vol. 199, Nov. 2021, Art. no. 110576.

[42] Y. Yu, J. Zhao, Q. Gong, C. Huang, G. Zheng, and J. Ma, "Real-time underwater maritime object detection in side-scan sonar images based on transformer-YOLOv5," *Remote Sens.*, vol. 13, no. 18, p. 3555, Sep. 2021.

[43] S. Li, Y. Li, Y. Li, M. Li, and X. Xu, "YOLO-FIRI: Improved YOLOv5 for infrared image object detection," *IEEE Access*, vol. 9, pp. 141861–141875, 2021.

[44] R. Perera, D. Guzzetti, and V. Agrawal, "Optimized and autonomous machine learning framework for characterizing pores, particles, grains and grain boundaries in microstructural images," *Comput. Mater. Sci.*, vol. 196, Aug. 2021, Art. no. 110524.

[45] E. Bisong, *Building Machine Learning And Deep Learning Models on Google Cloud Platform*, 2019, pp. 59–64.

[46] A. Paszke et al., "PyTorch: An imperative style, high-performance deep learning library," in *Proc. Adv. Neural Inf. Process. Syst.*, vol. 32, 2019, pp. 1–12.

[47] A. Paszke, S. Gross, S. Chintala, G. Chanan, E. Yang, Z. DeVito, Z. Lin, A. Desmaison, L. Antiga, and A. Lerer, "Automatic differentiation in PyTorch," Tech. Rep., 2017.

[48] S. Leuders, M. Thöne, A. Riemer, T. Niendorf, T. Tröster, H. A. Richard, and H. J. Maier, "On the mechanical behaviour of titanium alloy TiAl6 V4 manufactured by selective laser melting: Fatigue resistance and crack growth performance," *Int. J. Fatigue*, vol. 48, pp. 300–307, Mar. 2013.
[49] R. Snell, S. Tammas-Williams, L. Chechik, A. Lyle, E. Hernández-Nava, C. Boig, G. Panoutsos, and I. Todd, "Methods for rapid pore classification in metal additive manufacturing," *JOM*, vol. 72, no. 1, pp. 101–109, Jan. 2020.
[50] A. Thompson, I. Maskery, and R. K. Leach, "X-ray computed tomography for additive manufacturing: A review," *Meas. Sci. Technol.*, vol. 27, no. 7, Jul. 2016, Art. no. 072001.
[51] J. A. Slotwinski, E. J. Garboczi, P. E. Stutzman, C. F. Ferraris, S. S. Watson, and M. A. Peltz, "Characterization of metal powders used for additive manufacturing," *J. Res. Nat. Inst. Standards Technol.*, vol. 119, p. 460, Jan. 2014.
[52] J. A. Slotwinski and E. J. Garboczi, "Metrology needs for metal additive manufacturing powders," *JOM*, vol. 67, no. 3, pp. 538–543, Mar. 2015.
[53] E. Chlebus, B. Kuźnicka, R. Dziedzic, and T. Kurzynowski, "Titanium alloyed with rhenium by selective laser melting," *Mater. Sci. Eng., A*, vol. 620, pp. 155–163, Jan. 2015.
[54] H. Attar, L. Löber, A. Funk, M. Calin, L. C. Zhang, K. G. Prashanth, S. Scudino, Y. S. Zhang, and J. Eckert, "Mechanical behavior of porous commercially pure Ti and Ti–TiB composite materials manufactured by selective laser melting," *Mater. Sci. Eng., A*, vol. 625, pp. 350–356, Feb. 2015.
[55] J. V. Gordon, S. P. Narra, R. W. Cunningham, H. Liu, H. Chen, R. M. Suter, J. L. Beuth, and A. D. Rollett, "Defect structure process maps for laser powder bed fusion additive manufacturing," *Additive Manuf.*, vol. 36, Dec. 2020, Art. no. 101552.
[56] W. M. Tucho, V. H. Lysne, H. Austbø, A. Sjolyst-Kverneland, and V. Hansen, "Investigation of effects of process parameters on microstructure and hardness of SLM manufactured SS316L," *J. Alloys Compounds*, vol. 740, pp. 910–925, Apr. 2018.
[57] E. Liverani, S. Toschi, L. Ceschini, and A. Fortunato, "Effect of selective laser melting (SLM) process parameters on microstructure and mechanical properties of 316L austenitic stainless steel," *J. Mater. Process. Technol.*, vol. 249, pp. 255–263, Nov. 2017.
[58] F. Imani, R. Chen, E. Diewald, E. Reutzel, and H. Yang, "Deep learning of variant geometry in layerwise imaging profiles for additive manufacturing quality control," *J. Manuf. Sci. Eng.*, vol. 141, no. 11, Nov. 2019, Art. no. 111001.
[59] M. A. Ansari, A. Crampton, R. Garrard, B. Cai, and M. Attallah, "A convolutional neural network (CNN) classification to identify the presence of pores in powder bed fusion images," *Int. J. Adv. Manuf. Technol.*, vol. 120, nos. 7–8, pp. 5133–5150, Jun. 2022.
[60] C. Gobert, E. W. Reutzel, J. Petrich, A. R. Nassar, and S. Phoha, "Application of supervised machine learning for defect detection during metallic powder bed fusion additive manufacturing using high resolution imaging," *Additive Manuf.*, vol. 21, pp. 517–528, May 2018.
[61] K. Wasmer, T. Le-Quang, B. Meylan, and S. A. Shevchik, "In situ quality monitoring in AM using acoustic emission: A reinforcement learning approach," *J. Mater. Eng. Perform.*, vol. 28, no. 2, pp. 666–672, Feb. 2019.
[62] S. A. Shevchik, G. Masinelli, C. Kenel, C. Leinenbach, and K. Wasmer, "Deep learning for in situ and real-time quality monitoring in additive manufacturing using acoustic emission," *IEEE Trans. Ind. Informat.*, vol. 15, no. 9, pp. 5194–5203, Sep. 2019.
[63] O. Kwon, H. G. Kim, M. J. Ham, W. Kim, G.-H. Kim, J.-H. Cho, N. I. Kim, and K. Kim, "A deep neural network for classification of melt-pool images in metal additive manufacturing," *J. Intell. Manuf.*, vol. 31, no. 2, pp. 375–386, Feb. 2020.
[64] T. Kolb, L. Müller, J. Tremel, and M. Schmidt, "Melt pool monitoring for laser beam melting of metals: Inline-evaluation and remelting of surfaces," *Proc. CIRP*, vol. 74, pp. 111–115, Jan. 2018.
[65] L. Scime and J. Beuth, "Using machine learning to identify in-situ melt pool signatures indicative of flaw formation in a laser powder bed fusion additive manufacturing process," *Additive Manuf.*, vol. 25, pp. 151–165, Jan. 2019.
[66] M. A. Ansari, A. Crampton, and S. Parkinson, "A layer-wise surface deformation defect detection by convolutional neural networks in laser powder-bed fusion images," *Materials*, vol. 15, no. 20, p. 7166, Oct. 2022.
[67] Q. Guo, C. Zhao, M. Qu, L. Xiong, L. I. Escano, S. M. H. Hojjatzadeh, N. D. Parab, K. Fezzaa, W. Everhart, T. Sun, and L. Chen, "In-situ characterization and quantification of melt pool variation under constant input energy density in laser powder bed fusion additive manufacturing process," *Additive Manuf.*, vol. 28, pp. 600–609, Aug. 2019.
[68] P. Lhuissier, X. Bataillon, C. Maestre, J. Sijobert, E. Cabrol, P. Bertrand, E. Boller, A. Rack, J.-J. Blandin, L. Salvo, and G. Martin, "In situ 3D X-ray microtomography of laser-based powder-bed fusion (L-PBF)—A feasibility study," *Additive Manuf.*, vol. 34, Aug. 2020, Art. no. 101271.
[69] (2020). *Ultralytics YOLOv5*. Accessed: Dec. 3, 2022. [Online]. Available: https://github.com/ultralytics/yolov5
[70] N. H. Paulson, B. Gould, S. J. Wolff, M. Stan, and A. C. Greco, "Correlations between thermal history and keyhole porosity in laser powder bed fusion," *Additive Manuf.*, vol. 34, Aug. 2020, Art. no. 101213.
[71] N. P. Calta, J. Wang, A. M. Kiss, A. A. Martin, P. J. Depond, G. M. Guss, V. Thampy, A. Y. Fong, J. N. Weker, K. H. Stone, C. J. Tassone, M. J. Kramer, M. F. Toney, A. Van Buuren, and M. J. Matthews, "An instrument for in situ time-resolved X-ray imaging and diffraction of laser powder bed fusion additive manufacturing processes," *Rev. Sci. Instrum.*, vol. 89, no. 5, May 2018, Art. no. 055101.
[72] A. Bobel, L. G. Hector, I. Chelladurai, A. K. Sachdev, T. Brown, W. A. Poling, R. Kubic, B. Gould, C. Zhao, N. Parab, A. Greco, and T. Sun, "In situ synchrotron X-ray imaging of 4140 steel laser powder bed fusion," *Materialia*, vol. 6, Jun. 2019, Art. no. 100306.
[73] G. Kasperovich, J. Haubrich, J. Gussone, and G. Requena, "Correlation between porosity and processing parameters in TiAl6 V4 produced by selective laser melting," *Mater. Des.*, vol. 105, pp. 160–170, Sep. 2016.
[74] B. Shen, H. Li, S. Liu, J. Zou, S. Shen, Y. Wang, T. Zhang, D. Zhang, Y. Chen, and H. Qi, "Influence of laser post-processing on pore evolution of Ti–6Al–4 V alloy by laser powder bed fusion," *J. Alloys Compounds*, vol. 818, Mar. 2020, Art. no. 152845.
[75] N. T. Aboulkhair, M. Simonelli, L. Parry, I. Ashcroft, C. Tuck, and R. Hague, "3D printing of aluminium alloys: Additive manufacturing of aluminium alloys using selective laser melting," *Prog. Mater. Sci.*, vol. 106, Dec. 2019, Art. no. 100578.
[76] N. T. Aboulkhair, N. M. Everitt, I. Ashcroft, and C. Tuck, "Reducing porosity in AlSi10Mg parts processed by selective laser melting," *Additive Manuf.*, vols. 1–4, pp. 77–86, Oct. 2014.
[77] T. Sahar, M. Rauf, A. Murtaza, L. A. Khan, H. Ayub, S. M. Jameel, and I. U. Ahad, "Anomaly detection in laser powder bed fusion using machine learning: A review," *Results Eng.*, vol. 17, Mar. 2023, Art. no. 100803.
[78] A. M. Rinaldi, C. Russo, and C. Tommasino, "Automatic image captioning combining natural language processing and deep neural networks," *Results Eng.*, vol. 18, Jun. 2023, Art. no. 101107.

MUHAMMAD AYUB ANSARI received the bachelor's degree in computer science from Pakistan and the USA, in 2015, the master's degree from Bradford University, U.K., in 2018, and the Ph.D. degree in AI, in 2019, under the supervision of Prof. Andrew Crampton and Prof. Simon Parkinson.

In 2015, he developed a fascination with artificial intelligence (AI) and its incredible applications, inspiring him to further his education. His master's project involved developing a digital marketing solution for local businesses using natural language processing (NLP), which aimed to automate their advertising efforts. He is currently a Lecturer with the University of Huddersfield, focusing on computing and engineering. With over five years of experience in developing deep learning models, his work has contributed to the successful completion of two Innovate U.K. projects and has established fruitful collaborations with various international companies and colleagues. His research interests include detecting micro-defects in laser powder bed fusion processes using deep learning models, a project that held significant implications for improving quality assurance in metal additive manufacturing. Currently, his research revolves around applying computer vision techniques to enhance quality assurance in industrial 3D metal printing and to assist in cancer diagnosis through medical imaging.

ANDREW CRAMPTON received the bachelor's degree in mathematics and statistics from the University of Bradford, U.K., in 1999, and the Ph.D. degree in approximation theory from the University of Huddersfield, U.K., in 2002, under the supervision of Prof. John C. Mason.

His Ph.D. thesis mainly concentrated on the reconstruction of smooth surfaces from noisy and scattered data using radial basis function models. The title of thesis was "Radial Basis and Support Vector Machine Algorithms for Approximating Discrete Data." The problems that, he studied included randomly scattered, structured, and semi-structured data approximation using novel approximation estimators to mitigate the effects of outlier bias. He is currently a Professor of computational mathematics, an Associate Dean for Teaching and Learning, and a member of the Centre for Autonomous and Intelligent Systems, University of Huddersfield. He has successfully supervised more than ten Ph.D. students covering areas in disc-brake vibration analysis, SCADA systems, network security, 3D printing, neuro-fuzzy inference systems, and non-linear parameter estimation. He also works with colleagues on problems concerned with automated planning, such as knowledge extraction, knowledge representation, and automated planning for optimal multi-process control. His current research interest includes the applications of machine learning.

SIMON PARKINSON is currently a Professor of cyber security. He is also the Computer Science Department Research Coordinator. Outside of University, he trains and competes with Longwood Harriers AC. He has supervised seven research degrees (four Ph.D. students and three master's students by research) to completion as the Director of Studies and a further four as a second Supervisor (three Ph.D. students and one master's students by Research). He is passionate about leading research students to success and has twice been awarded the School Supervisor of the Year (2018–2019) and the overall University Supervisor of the Year, in 2020. He has examined eight Ph.D. students at both U.K. and international institutions. He has led various research and knowledge exchange projects to completion, exceeding the value of £1.5m, funded by the U.K. Engineering and Physical Science Research Council (EPSRC), the Defence Science and Technology Laboratory (DSTL), and Innovate U.K. His research interests include cyber security and artificial intelligence, with focused areas on identity and access. Through his research, he has developed new ways to detect security weaknesses in access control systems, intrusions in enterprise IT systems, and unauthorized access through new biometrics, such as key typing patterns and fitness devices.

He is a member of the U.K. Government's Cyber Security Advisory Board. He is an Associate Editor of *IET Intelligent Transport Systems*, a frequent program committee member for leading conferences, and a reviewer for many leading international journals.